

A Nodal Triangle-based Spectral Element Method for the Shallow Water Equations on the Sphere

F. X. Giraldo^{†1}, and T. Warburton[‡]

[†]*Naval Research Laboratory, Monterey, CA 93943*

[‡]*Department of Computational and Applied Mathematics, Rice University, Houston, TX 77005*

Submitted to the **Journal of Computational Physics**

August 16, 2004

A nodal triangle-based spectral element (SE) method for the shallow water equations on the sphere is presented. The original SE method uses quadrilateral elements and high-order nodal Lagrange polynomials, constructed from a tensor-product of the Legendre-Gauss-Lobatto points. In this work we construct the high-order Lagrange polynomials directly on the triangle using nodal sets obtained from the electrostatics principle [16] and Fekete points [22]. These nodes have good approximation properties and far better Lebesgue constants than the nodal set derived from equispaced points on the triangle. By employing triangular elements as the basic building-blocks of the SE method and the Cartesian coordinate form of the equations, we can use any grid imaginable including fully unstructured grids. Since the construction of nodal triangle-based SE methods may be new to many including those in the SE community we describe the details of constructing the cardinal basis functions, the differentiation and integration procedures, and the construction of filters required to maintain stability. An existing code that uses triangular finite elements can be extended to incorporate the high-order basis functions we describe herein. Results for six test cases are presented to confirm the accuracy and stability of the method. The results show that the triangle-based SE method yields the expected exponential convergence and that it is more accurate than the quadrilateral-based SE method even while using 30% to 60% fewer grid points. However, at the moment, the quadrilateral-based SE method is twice as fast as the triangle-based SE method.

Key Words: electrostatics, Delaunay, Fekete, grid, icosahedron, Jacobi, Lagrange, nodal, polynomial, quadrilateral, shallow water equations, spectral element method, spherical geometry, triangle.

¹Corresponding Author

1. INTRODUCTION

The recent trend towards distributed-memory computers having thousands of commodity processors has rekindled interest in the development of local high-order methods for the simulation of geophysical fluid dynamics applications. The most common local high-order method is the spectral element (SE) method. The SE method can be constructed in modal (spectral) or nodal (physical) space. In addition, the building-blocks (or element shapes) used for the SE method have been the quadrilateral or the triangle. If quadrilaterals are used then the SE method is employed in nodal space where the basis functions are constructed from a tensor-product of the one-dimensional Legendre cardinal functions [15]. However, if triangles are used then the SE method has been typically employed only in modal space [19]. This was due to the lack of a good set of nodal points for the triangle.

Using the electrostatics principle, Hesthaven [16] obtained a set of nodal points on the triangle with good approximation properties for all polynomials of order $N < 11$. For $11 \leq N \leq 15$ we use the Fekete points [22] which are only currently available for orders $N < 20$. Using this nodal set on the triangle and the SE method Warburton et al. [23] showed exponential convergence for the incompressible Navier-Stokes equations. The success of these results has inspired us to seek similarly successful applications of this nodal triangular set for the solution of the shallow water equations on the sphere.

The shallow water equations are a set of first order nonlinear hyperbolic equations which contain all of the horizontal operators found in the primitive atmospheric equations used in numerical weather prediction (NWP) and climate models. Thus to design a good atmospheric model requires a good shallow water model. The construction of fast, accurate, and flexible atmospheric models is the ultimate goal of our research. In this quest, we have successfully developed an exponentially convergent global atmospheric model using the nodal quadrilateral-based SE method [12, 13]. While the accuracy and performance of this model have been shown to exceed those of operational spectral transform models [13], developing adaptive grids for quadrilateral elements may prove too cumbersome to pursue. The existence of numerous adaptive triangular mesh generation packages [1, 8] motivates us to explore nodal triangle-based SE methods.

The remainder of the paper is organized as follows. Section 2 describes the governing equations of motion used to test our numerical method. In Sec. 3 we describe the discretization of the governing equations. This includes the spatial discretization by the triangle-based SE method and the time-integrator. In Sec. 4 we describe a few of the many possible triangular tessellations of the sphere. Finally, in Sec. 5 we present convergence rates of the nodal triangle-based SE method and compare it with the quadrilateral-based SE method. This then leads to some conclusions about the feasibility of this approach for constructing future atmospheric models and a discussion on the direction of future work.

2. SHALLOW WATER EQUATIONS

The shallow water equations are a system of first order nonlinear hyperbolic equations which govern the motion of an inviscid incompressible fluid in a shallow depth. The predominant feature of this type of fluid is that the characteristic length

of the fluid is far greater than its depth which is analogous to the motion of air in the atmosphere and water in the oceans. For this reason these equations are typically used as a first step toward the construction of either NWP, climate, or ocean models.

The spherical shallow water equations in Cartesian advective form are

$$\frac{\partial \phi}{\partial t} + \nabla \cdot (\phi \mathbf{u}) = 0 \quad (1)$$

$$\frac{\partial \mathbf{u}}{\partial t} + \mathbf{u} \cdot \nabla \mathbf{u} = -f(\mathbf{x} \times \mathbf{u}) - \nabla(\phi + \phi^s) - \mu \mathbf{x}, \quad (2)$$

where the nabla operator is defined as $\nabla = (\partial_x, \partial_y, \partial_z)^T$, ϕ is the geopotential height ($\phi = gh$ where g is the gravitational constant and h is the vertical height of the fluid), ϕ^s is the surface topography (e.g., mountains), $\mathbf{u} = (u, v, w)^T$ is the Cartesian wind velocity vector, $f = \frac{2\omega z}{a}$ is the Coriolis parameter and (ω, a) represent the rotation of the earth and its radius, respectively.

The term $\mu \mathbf{x}$, where $\mathbf{x} = (x, y, z)^T$ is the position vector of the grid points, is a fictitious force introduced to constrain the fluid particles to remain on the surface of the sphere. By switching from spherical (2D) to Cartesian (3D) coordinates we have allowed the fluid particles an additional degree of freedom which will manifest itself in the fluid particles flying off the surface of the sphere. In order to prevent this from happening we introduce the Lagrange multiplier μ .

The shallow water equations in Cartesian form have received significant attention recently (see [7, 9, 10, 11, 14, 21]). It should be mentioned that the Cartesian form of the equations introduces no approximations whatsoever; the equations are completely equivalent to the equations in spherical coordinates as shown by Swartrauber et al. [21]. The reason for using the Cartesian form of the equations is that the pole singularity associated with spherical coordinates is avoided and because this form, in conjunction with the SE mapping described in Sec. 3.1.2, allows for any curved surface to be discretized by this approach. For example, we could easily change the shape of the spherical domain to any warped spheroidal. This will allow for a more realistic representation of the earth since it is not a perfect sphere.

3. DISCRETIZATION

In this section we describe the discretization of the shallow water equations. In Sec. 3.1, we describe the spatial discretization by the spectral element method including: the mapping from physical 3D Cartesian space to the local 2D reference space, the choice of basis functions, differentiation, integration, and the filter used to maintain stability. In Sec. 3.2 we discuss the explicit time-integrator, the time-filter used to control the computational modes, and the Lagrange multiplier required to constrain the fluid particles onto the sphere.

3.1. Spatial Discretization by the Triangle-based Spectral Element Method

3.1.1. Background and Motivation

To explain the need for the electrostatics and Fekete points on the triangle a few words regarding interpolation theory are required. Let P_N denote the space of all

polynomials of degree $\leq N$ and ξ_i be a collection of points in P_N . In addition, let q be an arbitrary function that we wish to interpolate and I_N an unique function in P_N such that $I_N(q(\xi_i)) = q(\xi_i)$. Using the usual definition of the L_∞ norm

$$\| q \| = \max_{\xi \in \Omega} | q(\xi) |$$

$$\| I_N \| = \max_{\| q \| = 1} | I_N(q) |$$

we can now quantify the error of approximating q by $I_N(q)$ within the triangle Ω . Assuming the existence of a function $r \in P_N$ which best approximates q and noting that we can write $r = I_N(r)$ we can compute the interpolation error of q as

$$\| q - I_N(q) \| = \| q - r + I_N(r) - I_N(q) \|.$$

Using the Cauchy-Schwarz inequality yields

$$\| q - I_N(q) \| \leq (1 + \| I_N \|) \| q - r \| \quad (3)$$

where $\| I_N \|$ denotes the Lebesgue constant which must be minimized in order to avoid the well-known Runge effect [19] typical of monomial expansions of the type $\xi^i \eta^j$ | $0 \leq i + j \leq N$; these expansions become approximately linearly dependent and hence quite ill-conditioned. This is the expansion typically associated with the standard finite element method where the points (ξ, η) are equi-spaced within the triangle. Since it is not known how to compute Lebesgue points (i.e., points which minimize the Lebesgue constant) we use points computed via an electrostatics analogy or points which maximize the determinant of the Vandermonde matrix (Fekete points) which indirectly approximate them. On the 1-simplex (the line $\xi \in [-1, +1]$) the points satisfying the electrostatics and Fekete principles are in fact the Legendre-Gauss-Lobatto (LGL) points. However, on the 2-simplex (the triangle $-1 \leq \xi, \eta \leq 1$; $\xi + \eta \leq 0$) determining which are the optimal points remains an open question. Nonetheless, attempts have been made to construct nodal sets which yield LGL points along the edges of the triangle. Both the electrostatics and Fekete points satisfy this condition and the fact that they have good Lebesgue constants make them suitable choices for constructing triangle-based spectral element basis functions. The Fekete and electrostatics points coincide with the standard equi-spaced points for $N \leq 2$. However, the Lebesgue constant for the Fekete ($\forall N$) and electrostatics points ($N < 9$) increases proportionally with N while for the standard equi-spaced points the Lebesgue constant increases exponentially with N .

The term $\| q - r \|$ in Eq. (3) is minimized if the polynomial space P_N is able to approximate the function q . For the triangle this is in fact the case if the Koornwinder-Dubiner polynomials [5, 17] are used as these are the natural bases on the triangle. The construction of the cardinal functions based on the Koornwinder polynomials is the topic of the next section. In this section, we have only discussed the interpolation properties of certain nodal sets and bases, however, in order to construct discrete operators requires not only good interpolation properties but also good integration properties.

On the 1-simplex the LGL points happen to be both optimal interpolation and integration points which results in a diagonal mass matrix since the interpolation

and integration points are co-located; having a diagonal mass matrix is important for achieving efficiency. On the 2-simplex such points have not yet been found and thus far one must be content to choose either good interpolation or integration but not both. In this paper we choose good interpolation and then use exact numerical integration formulas (cubature) which, while quite accurate, does not result in a diagonal or lumpable mass matrix, since the interpolation and integration points are not co-located.

3.1.2. Basis Functions

To define the local operators which shall be used to construct the global approximation of the solution we begin by decomposing the spherical domain Ω into N_e non-overlapping triangular elements Ω_e such that

$$\Omega = \bigcup_{e=1}^{N_e} \Omega_e.$$

To perform differentiation and integration operations, we introduce the nonsingular mapping $\mathbf{x} = \Psi(\boldsymbol{\xi})$ which defines a transformation from the physical Cartesian coordinate system $\mathbf{x} = (x, y, z)^T$ to the local reference coordinate system $\boldsymbol{\xi} = (\xi, \eta, \zeta)$ such that (ξ, η) lies on the spherical surface tiled by the triangular elements defined by $\Omega_e = \{(\xi, \eta, \zeta), -1 \leq \xi, \eta \leq 1, \xi + \eta \leq 0, \zeta = 1\}$.

Associated with the local mapping, Ψ , is the transformation Jacobian, $J = \frac{\partial \mathbf{x}}{\partial \boldsymbol{\xi}}$, and the determinant

$$|J| = \frac{\partial \mathbf{x}}{\partial \zeta} \cdot \mathbf{G}, \quad \mathbf{G} = \frac{\partial \mathbf{x}}{\partial \xi} \times \frac{\partial \mathbf{x}}{\partial \eta},$$

where \mathbf{G} represents the surface conforming component of the mapping (see Giraldo [9] for further details).

We can now use this mapping to define the local representation of the solution, $\mathbf{q} = (\phi, \mathbf{u}^T)^T$, and the approximation of operations such as differentiation and integration. For simplicity, we assume ζ to be unity in what remains and denote $\boldsymbol{\xi} = (\xi, \eta)$.

Let us now represent the local element-wise solution \mathbf{q} by an N th order polynomial in $\boldsymbol{\xi}$ as

$$\mathbf{q}_N(\boldsymbol{\xi}) = \sum_{k=1}^{M_N} L_k(\boldsymbol{\xi}) \mathbf{q}_N(\boldsymbol{\xi}_k)$$

where $\boldsymbol{\xi}_k$ represents $M_N = \frac{1}{2}(N+1)(N+2)$ grid points and $L_k(\boldsymbol{\xi})$ are the associated multivariate Lagrange polynomials. For the grid points (ξ_i, η_j) we choose the nodal set derived from the electrostatics principle [16] for $N < 11$ and the Fekete points for $11 \leq N \leq 15$.

We construct the Lagrange polynomials on the reference triangle, $L_k(\xi, \eta)$, which are implicitly defined by their cardinal nature, by reference to an easily constructed orthonormal Koornwinder-Dubiner polynomial basis [5, 17]. This basis is defined as

$$\psi_k(\xi, \eta) = \sqrt{\frac{(2i+1)(i+j+1)}{2}} P_i^{0,0} \left(\frac{2\xi + \eta + 1}{1 - \eta} \right) \left(\frac{1 - \eta}{2} \right)^i P_j^{2i+1,0}(\eta) \quad (4)$$

where $P_n^{\alpha,\beta}(\xi)$ represents the n th order Jacobi polynomial in the interval $\xi \in [-1, +1]$, $k = i + j(N + 1) + 1$, and the indices vary as $0 \leq i, j; i + j \leq N$, and $k = 1, \dots, M_N$.

We now seek an explicit formula for the Lagrange basis by representing them in terms of the reference basis, i.e.

$$L_i(\xi, \eta) = \sum_{k=1}^{M_N} A_{ik} \psi_k(\xi, \eta) \quad (5)$$

where the indices are now defined as $i, j, k = 1, \dots, M_N$. We then use the cardinal property of the Lagrange polynomials

$$\delta_{ij} = \sum_{k=1}^{M_N} A_{ik} \psi_k(\xi_j, \eta_j),$$

where δ is the Kronecker delta function, to determine that

$$A_{ik} = (\psi_k^{-1}(\xi_i, \eta_i))^T. \quad (6)$$

We next recognize that

$$V_{jk} = \psi_k(\xi_j, \eta_j) \quad (7)$$

is a generalized Vandermonde matrix and using Eqs. (5), (6), and (7) we construct the Lagrange polynomials as follows

$$L_i(\xi, \eta) = \sum_{k=1}^{M_N} (V^{-1})_{ik}^T \psi_k(\xi, \eta). \quad (8)$$

We note that, for example, the Vandermonde matrix generated using this basis and the 15th order Fekete nodes only has a condition number of approximately 116. This good conditioning allows us to use this approach in contrast to conventional wisdom regarding poor conditioning of the standard monomial based Vandermonde.

3.1.3. Differentiation

Writing Eq. (8) in matrix form

$$\mathbf{L} = (\mathbf{V}^{-1})^T \boldsymbol{\psi} \quad (9)$$

one can show that the differentiation matrices in the reference coordinate system are defined as

$$\frac{\partial \mathbf{L}}{\partial \xi} = \mathbf{D}_\xi, \quad \frac{\partial \mathbf{L}}{\partial \eta} = \mathbf{D}_\eta, \quad \frac{\partial \mathbf{L}}{\partial \zeta} = \mathbf{D}_\zeta$$

where

$$\mathbf{D}_\xi = (\mathbf{V}^{-1})^T \frac{\partial \boldsymbol{\psi}}{\partial \xi}, \quad \mathbf{D}_\eta = (\mathbf{V}^{-1})^T \frac{\partial \boldsymbol{\psi}}{\partial \eta}, \quad \mathbf{D}_\zeta = (\mathbf{V}^{-1})^T \boldsymbol{\psi} = \mathbf{L}. \quad (10)$$

Using Eq. (10) and the chain rule one can show that the derivatives in the physical Cartesian coordinate system are defined as follows

$$\begin{aligned}\frac{\partial \mathbf{L}}{\partial x} &= \mathbf{D}_\xi \frac{\partial \xi}{\partial x} + \mathbf{D}_\eta \frac{\partial \eta}{\partial x} + \mathbf{D}_\zeta \frac{\partial \zeta}{\partial x} \\ \frac{\partial \mathbf{L}}{\partial y} &= \mathbf{D}_\xi \frac{\partial \xi}{\partial y} + \mathbf{D}_\eta \frac{\partial \eta}{\partial y} + \mathbf{D}_\zeta \frac{\partial \zeta}{\partial y} \\ \frac{\partial \mathbf{L}}{\partial z} &= \mathbf{D}_\xi \frac{\partial \xi}{\partial z} + \mathbf{D}_\eta \frac{\partial \eta}{\partial z} + \mathbf{D}_\zeta \frac{\partial \zeta}{\partial z}\end{aligned}$$

where $\frac{\partial \xi}{\partial x}$ are just the components of the inverse Jacobian matrix J^{-1} (for details see Giraldo [9]).

3.1.4. Filtering the High-Frequency Waves

Recall that the local element-wise Vandermonde matrix can be written as

$$V_{ij} = \psi_j(\xi_i, \eta_i).$$

Thus the function values at each grid point i inside the element Ω_e can be defined, using a modal (spectral) expansion, as follows

$$q_i = \sum_{j=1}^{M_N} \psi_j(\xi_i, \eta_i) \tilde{q}_j \quad (11)$$

where \tilde{q} represents the expansion coefficients in modal space of the function q . In matrix form we can write Eq. (11) as

$$\mathbf{q} = \mathbf{V} \tilde{\mathbf{q}} \quad (12)$$

which we call the nodal triangle-based SE transform because it allows us to transform from nodal to modal space. Inverting Eq. (12) yields

$$\tilde{\mathbf{q}} = (\mathbf{V}^{-1}) \mathbf{q}$$

which yields the amplitudes in the modal representation (amplitude-frequency space). We can then filter these amplitudes in any manner but here, based on past experience [10, 12], we choose the Boyd-Vandeven transfer function [2] which we denote by Λ . Applying the filter to the amplitudes and then transforming to nodal (physical) space is achieved in the following matrix-vector multiply operation

$$\mathbf{q}^F = \mathbf{F} \mathbf{q}$$

where

$$\mathbf{F} = \mathbf{V} \Lambda (\mathbf{V}^{-1}) \quad (13)$$

is the $M_N \times M_N$ filter matrix. This filter matrix is applied every 10 time-steps.

3.1.5. Integration

In order to complete the discussion of the local element-wise operations required to construct discrete spectral element operators we must lastly describe the integration procedure required by the weak formulation of all Galerkin methods. For any two functions f and g the integration \mathcal{I} proceeds as follows

$$\mathcal{I}[f, g] = \int_{\Omega_e} f(\mathbf{x}) g(\mathbf{x}) d\mathbf{x} = \sum_{i=1}^{M_Q} w_i |J(\boldsymbol{\xi}_i)| f(\boldsymbol{\xi}_i) g(\boldsymbol{\xi}_i)$$

where M_Q is a function of Q - the order of the cubature approximation. For w_i and $\boldsymbol{\xi}_i$ we use the high-order cubature rules for the triangle given in [20, 3, 4] of order $2N$. This order is chosen for two reasons: first, it is a good compromise between accuracy and efficiency; and second, it allows for a fair comparison of our new triangle-based SE method with the quadrilateral-based SE method which typically uses order $2N - 1$ quadrature rules.

3.1.6. Local Element-wise Operators

To simplify the description of the numerical algorithm, let us define the following local element operators: let

$$M_{ij}^e = \int_{\Omega_e} L_i(\mathbf{x}) L_j(\mathbf{x}) d\mathbf{x} \quad (14)$$

represent the mass matrix,

$$\mathbf{D}_{ijk}^e = \int_{\Omega_e} L_i(\mathbf{x}) L_j(\mathbf{x}) \nabla L_k(\mathbf{x}) d\mathbf{x} \quad (15)$$

the differentiation matrix,

$$\mathbf{G}_{ij}^e = \int_{\Omega_e} L_i(\mathbf{x}) \nabla L_j(\mathbf{x}) d\mathbf{x} \quad (16)$$

the gradient matrix, and

$$C_{ijkl}^e = \int_{\Omega_e} L_i(\mathbf{x}) L_j(\mathbf{x}) L_k(\mathbf{x}) L_l(\mathbf{x}) d\mathbf{x} \quad (17)$$

the Coriolis matrix where $i, j, k, l = 1, \dots, M_N$. Note that $\mathbf{D}^e = (D_x^e, D_y^e, D_z^e)$ and $\mathbf{G}^e = (G_x^e, G_y^e, G_z^e)$ are vectors of matrices corresponding to the three spatial directions.

3.1.7. Satisfying the Equations Globally

To satisfy the equations globally requires summing the local element matrices, Eqs. (14) - (17), to form their global representation. This summation procedure is known as the global assembly or direct stiffness summation. Let us represent this global assembly procedure by the summation operator

$$\bigwedge_{e=1}^{N_e}$$

with the mapping $(i, e) \longrightarrow (I)$ where $i = 1, \dots, M_N$ are the local element grid points, $e = 1, \dots, N_e$ are the spectral elements covering the spherical shell, and $I = 1, \dots, N_p$ are the global grid points. Applying the global assembly operator to the local element matrices results in the following global matrices:

$$M = \bigwedge_{e=1}^{N_e} M^e, \quad D = \bigwedge_{e=1}^{N_e} D^e, \quad G = \bigwedge_{e=1}^{N_e} G^e, \quad C = \bigwedge_{e=1}^{N_e} C^e.$$

With these operators defined and by denoting the global grid vector for the grid points as \mathbf{x} , the geopotential as ϕ , and the wind velocity as \mathbf{u} we can now state the variational form of the problem as: find $(\phi, \mathbf{u}^T)^T \in H^1(\Omega) \forall L \in H^1$ such that

$$M \frac{\partial \phi}{\partial t} + (D\phi)^T \mathbf{u} = - (D^T \mathbf{u}) \phi \quad (18)$$

$$M \frac{\partial \mathbf{u}}{\partial t} + (D\mathbf{u})^T \mathbf{u} = -Cf(\mathbf{x} \times \mathbf{u}) - G(\phi + \phi^s) - M(\mu \mathbf{x}) \quad (19)$$

where $H^1(\Omega)$ is the space of all functions with functions and first derivatives belonging to $L^2(\Omega)$ - the space of all functions that are square integrable over Ω . For ϕ and \mathbf{u} we choose the polynomial space P_N - P_N without violating the inf-sup condition.

3.2. Time-Integrator and the Lagrange Multiplier

Discretizing the equations in time by the leapfrog method yields

$$M\phi^{n+1} = M\phi^{n-1} - 2\Delta t \left((D\phi)^T \mathbf{u} + D^T \mathbf{u} \phi \right)^n \quad (20)$$

$$\begin{aligned} M\mathbf{u}^{n+1} = M\mathbf{u}^{n-1} & - 2\Delta t \left((D\mathbf{u})^T \mathbf{u} + Cf(\mathbf{x} \times \mathbf{u}) \right)^n \\ & - 2\Delta t (G(\phi + \phi^s) + M(\mu \mathbf{x}))^n. \end{aligned} \quad (21)$$

Since we need to ensure that the velocity field remains tangential to the sphere, we require

$$\mathbf{x} \cdot \mathbf{u} = 0.$$

Let us first write Eq. (21) as

$$\mathbf{u}^{n+1} = M^{-1} \mathbf{B}_u - 2\Delta t \mu \mathbf{x}, \quad (22)$$

where

$$\mathbf{B}_u = M\mathbf{u}^{n-1} - 2\Delta t \left((D\mathbf{u})^T \mathbf{u} + Cf(\mathbf{x} \times \mathbf{u}) \right)^n - 2\Delta t (G(\phi + \phi^s))^n.$$

Taking the scalar product of Eq. (22) with \mathbf{x} , and rearranging yields

$$\mu = \frac{1}{2\Delta t a^2} \mathbf{x} \cdot (M^{-1} \mathbf{B}_u). \quad (23)$$

Using Eq. (23) we note that we can project any 3D vector \mathbf{q} onto the surface of the sphere by applying the following matrix operator

$$P\mathbf{q} = \mathbf{q} - \frac{1}{a^2}(\mathbf{x} \cdot \mathbf{q})\mathbf{x} \quad (24)$$

where the projection matrix P is given by

$$P = \frac{1}{a^2} \begin{pmatrix} a^2 - x^2 & -xy & -xz \\ -xy & a^2 - y^2 & -yz \\ -xz & -yz & a^2 - z^2 \end{pmatrix}. \quad (25)$$

This allows the equations in constrained form to be written as follows

$$M\phi^{n+1} = M\phi^{n-1} - 2\Delta t \left((D\phi)^T \mathbf{u} + D^T \mathbf{u} \phi \right)^n \quad (26)$$

$$M\mathbf{u}^{n+1} = MPM^{-1}\mathbf{B}_u. \quad (27)$$

3.2.1. Time-Filter

To complete the discussion of the time-integrator, we must describe the Asselin filter used for the leapfrog method which otherwise would admit a nonphysical mode to propagate in the opposite direction from the physical mode. This filter is applied as follows

$$\mathbf{q}^n = \tilde{\mathbf{q}}^n + \gamma (\tilde{\mathbf{q}}^{n+1} - 2\tilde{\mathbf{q}}^n + \mathbf{q}^{n-1}) \quad (28)$$

where the tilde represents the unfiltered solution and $\gamma = 0.01$ is the filter strength. While it is true that for $\gamma \neq 0$ the leapfrog method becomes first order, we have used this time-integrator because it is typically used in atmospheric and shallow water models which will then facilitate comparisons with other methods. For more suitable time-integrators for the shallow water and atmospheric equations the reader is referred to the recent paper [13].

4. GRID GENERATION ON THE SPHERE

The choice of which triangulation to use for the sphere is not obvious. Commonly, grids are chosen which simplify the construction of the discrete operators. For example, latitude-longitude grids are used with spectral transform methods because these are the only grids that can be used with this method. The hexahedral grid (i.e., the cubed-sphere) has been used with finite difference and spectral element methods because each of the six faces of the cube map onto a simple Cartesian geometry that allows for the simple and rapid construction of the discrete operators. Picking one grid and constructing the discrete operators on a specific grid geometry simplifies matters but it also dictates the algorithm thereby losing any hope of using other types of grids and adaptive solution strategies.

In our case, the spectral element method is constructed in a very general way such that the model reads in any grid geometry and then constructs the discrete operators directly on the grid. This allows the use of any grid and offers the freedom to choose the best possible grid for specific applications. For the purposes

of validating the triangle-based SE method we shall use a disjointed set of triangles formed by the subdivision of the triangular faces of an icosahedron; however, it should be understood that any triangular grid can be used. We shall compare the triangle-based SE method with the quadrilateral-based SE method described in [9, 11, 12]. With the quadrilateral-based SE method we used hexahedral and icosahedral grids. The choice of hexahedral grids is a natural one because it represents a structured grid that has become quite popular with many newly proposed grid point methods. The quadrilateral-based icosahedral grid is chosen because it is an unstructured grid and represents a good comparison for the triangle-based icosahedral grid. Finally, to illustrate the geometric flexibility of the triangle-based SE method we describe a number of triangular unstructured grids formed by the Delaunay triangulation of various point sets.

4.1. Triangle-based Icosahedral Grids

To construct icosahedral grids we consider the initial icosahedron and subdivide each of the initial triangles by a triangular Lagrange polynomial of order n_I . Prior to mapping these elements onto the sphere it is convenient to map the triangles onto a gnomonic space. The most unbiased mapping is obtained by mapping about the centroid of the triangles.

Let (λ_c, φ_c) be the centroid of the triangle we wish to map where λ represents the zonal (east-west) and φ the meridional (north-south) directions. The gnomonic mapping is then given by

$$\begin{aligned} X &= \frac{a \cos \varphi \sin(\lambda - \lambda_c)}{\sin \varphi_c \sin \varphi + \cos \varphi_c \cos \varphi \cos(\lambda - \lambda_c)}, \\ Y &= \frac{a [\cos \varphi_c \sin \varphi - \sin \varphi_c \cos \varphi \cos(\lambda - \lambda_c)]}{\sin \varphi_c \sin \varphi + \cos \varphi_c \cos \varphi \cos(\lambda - \lambda_c)} \end{aligned} \quad (29)$$

where $\mathbf{X} \in [-1, +1]^2$ in the equi-distant gnomonic space G. To simplify matters a bit, we first apply a rotation whereby Eq. (29) becomes

$$X = a \tan \lambda_R, \quad Y = a \tan \varphi_R \sec \lambda_R, \quad (30)$$

in the new coordinate system with the centroid (λ_c, φ_c) located at $(0, 0)$. The rotation mapping is given as

$$\begin{aligned} \lambda_R &= \arctan \left[\frac{\cos \varphi \sin(\lambda - \lambda_c)}{\sin \varphi_c \sin \varphi + \cos \varphi_c \cos \varphi \cos(\lambda - \lambda_c)} \right], \\ \varphi_R &= \arcsin [\cos \varphi_c \sin \varphi - \sin \varphi_c \cos \varphi \cos(\lambda - \lambda_c)]. \end{aligned} \quad (31)$$

This approach enables the construction of a triangle-based icosahedral grid with the following properties

$$N_p = 10(n_I N)^2 + 2, \quad (32)$$

$$N_e = 20(n_I)^2, \quad (33)$$

where N_p and N_e denote the number of points and elements comprising the triangular grid, and n_I controls the number of triangular elements while N denotes

the order of the polynomial inside each element.

Table I and Fig. 1 provide

TABLE I
The number of grid points, N_p , and elements, N_e , for the triangle-based icosahedral grid as a function of n_I and N .

n_I	N	N_p	N_e
2	1	42	80
2	2	162	80
2	4	642	80
2	6	1446	80
2	8	2562	80
2	10	4002	80
2	12	5762	80
2	14	7842	80
3	8	5762	180
4	8	10242	320
5	8	16002	500

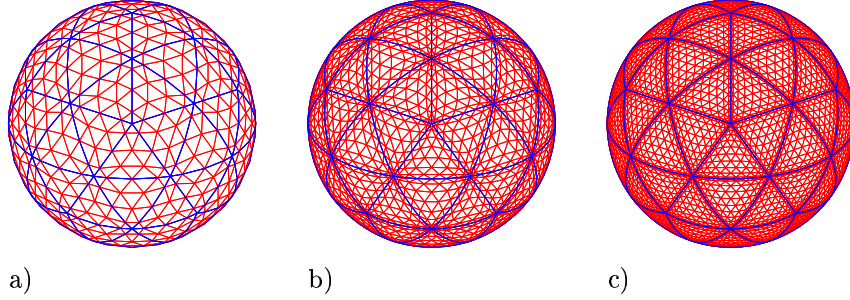


FIG. 1. Triangle-based icosahedral grid for $n_I = 2$ and a) $N = 4$, b) $N = 8$, and c) $N = 12$.

examples of grids for various values of N for n_I . All the grids illustrated are viewed from the North Pole where the thick lines denote the elements and the thin lines are the high-order grid points.

Since we use the icosahedral grid to compare the triangle-based SE method with the standard quadrilateral-based SE method on icosahedral and hexahedral grids it is important to compare grids with comparable total grid points. From [12] the number of points for the quad-based icosahedral and hexahedral grids are given as

$$N_p = 60(n_I^Q N)^2 + 2 \quad (34)$$

and

$$N_p = 6(n_H^Q N)^2 + 2 \quad (35)$$

where n_I^Q and n_H^Q are parameters which control the number of elements in the grids. Equating Eqs. (32), (34), and (35) shows that the triangle-based icosahedral

grid has the same number of grid points as the quadrilateral-based grids for

$$n_I = \sqrt{6} n_I^Q = \sqrt{\frac{6}{10}} n_H^Q \quad (36)$$

which we approximate by $n_I \sim 2n_I^Q \sim \frac{2}{3}n_H^Q$. Thus $n_I^Q = 1$, $n_H^Q = 3$, $n_I = 2$ should yield approximately the same number of grid points.

It should be mentioned that these grid constructions do not actually yield the same number of grid points and elements. In fact for this set of grid constructions the triangle-based icosahedral grid has 80 triangular elements while the quadrilateral-based icosahedral and hexahedral grids have 60 and 54, respectively. Although for a given polynomial order (N) they all span the same polynomial space within each element they differ greatly in the total number of grid points and in their distribution. In fact, the triangle-based icosahedral grid has 33% fewer points than the quad-based icosahedral grid and 25% fewer points than the quad-based hexahedral grid. In addition, the triangle-based grid appears to be far more isotropic than the quadrilateral grids. In other words, the triangle-based icosahedral grid has no biasing in its orientation and thereby treats all directions equally. Unlike the quadrilateral-based icosahedral grid, the quadrilateral-based hexahedral grid is structured and isotropic but only along two directions in each of the six faces of the hexahedron. Therefore, the hexahedral grid will do quite well for flows which are aligned with these two directions. We shall see that some of the test cases benefit from this type grid orientation while others do not.

4.2. Triangulations Based on the Platonic Solids

In the previous section we described the construction of triangular grids using the icosahedron. However, there is nothing special about this Platonic solid; we could have used any of the five Platonic solids. For example, one could use the tetrahedron (4 triangular faces), hexahedron (6 quadrilateral faces), octahedron (8 triangular faces), dodecahedron (12 pentagonal faces), or icosahedron (20 triangular faces). However, the faces of the hexahedron and dodecahedron need to be subdivided into triangular elements (24 for the hexahedron and 60 for the dodecahedron). Using the Platonic solids one can create a grid with the following properties

$$N_p = \frac{N_T}{2}(n N)^2 + 2 \quad (37)$$

$$N_e = N_T n^2 \quad (38)$$

where N_T are the number of initial triangles comprising the Platonic solid and n is the subdivision of each of the initial triangles. $N_T = 4, 8, 20, 24$, and 60 for the tetrahedron, octahedron, icosahedron, hexahedron, and dodecahedron, respectively. In Fig. 2 we show equivalent resolution triangulations using the octahedron, icosahedron, and hexahedron viewed from the North Pole. From Fig. 2 it is evident that the octahedral and icosahedral grids are more uniform than the hexahedral grid; this is due to the fact that the initial triangles of the octahedron and icosahedron are equilateral triangles whereas those for the hexahedron are isosceles triangles. However, there are hardly any differences between these sets of grids but due to the popularity of icosahedral grids we shall use this set in Sec. 5 but it should be understood that all these grids yield similar convergence rates.

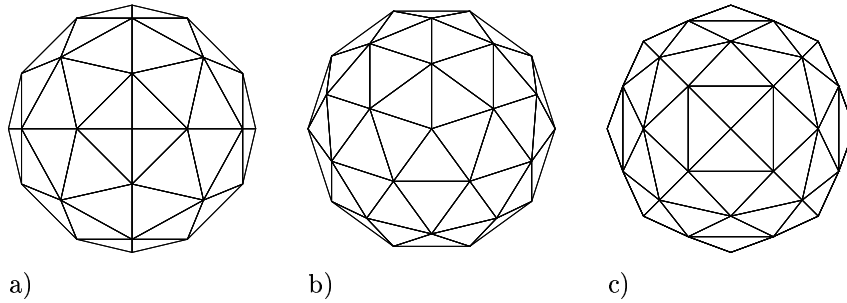


FIG. 2. Triangulations of the sphere using the a) octahedron ($N_e = 64$), b) icosahedron ($N_e = 80$), and c) hexahedron ($N_e = 96$) viewed from the North Pole.

4.2.1. Triangulations Based on Latitude-Longitude

Because triangles are the 2-simplex this means one can construct a unique triangulation for random point sets distributed on the surface of the sphere. This then facilitates the construction of triangulations on the sphere because as long as one can create point sets they can be triangulated quite naturally using Delaunay triangulation methods. For the latitude-longitude grids we use the STRIPACK Delaunay triangulation software [18].

In this section we discuss a few of the many possible triangular grids that can be constructed on the sphere. We limit the grids to fixed unstructured grids; that is, grids that are constructed at the beginning of the time-integration and remain fixed for all time. In the future we shall address the dynamically adaptive approach.

Latitude-Longitude grids are perhaps the simplest tessellations for the sphere. In fact, they are popular for NWP and climate models because these are the only grids that spectral transform methods can use. Figure 3a shows a *regular* latitude-longitude grid with $(N_{lon}, N_{lat}) = (40, 20)$. On each latitude ring (East-West direction) this grid has the same number of points ($N_{lon} = 40$) and the grid spacing becomes smaller as we approach the poles. This situation is known as the *pole problem* because there are too many redundant points near the poles as is illustrated by the lines of constant longitude (vertical) as they curve toward the poles. In addition, the proximity of adjacent points near the poles severely restricts the maximum time-step that can be used. One way around this dilemma is to use *thin* grids. As we approach the poles, the number of points on each latitude ring is decreased in order to maintain a constant grid spacing throughout. This type of grid is depicted in Fig. 3b where lines of constant longitude no longer curve toward the poles. Both the regular and thin latitude-longitude grids can be used with the spectral transform method (without the triangular elements). However, if the discretization method is based on triangles, then we can go even further and refine the region of interest and use a coarse grid everywhere else. Figure 3c shows an adaptive grid where the region of interest is along the Equator. We shall use this grid to show the advantages that adaptive unstructured triangular grids may offer.

5. NUMERICAL EXPERIMENTS

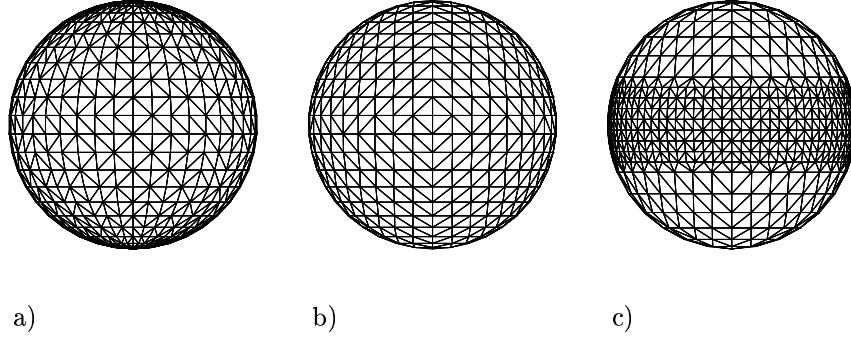


FIG. 3. Triangulations of the sphere using the following types of latitude-longitude grids: a) regular ($N_e = 1600$), b) thin ($N_e = 1044$), and c) adaptive ($N_e = 1844$) viewed from $(0,0)$.

For the numerical experiments, we use the normalized L_2 error norm

$$\|\phi\|_{L_2} = \sqrt{\frac{\int_{\Omega} (\phi_{\text{exact}} - \phi)^2 d\Omega}{\int_{\Omega} \phi_{\text{exact}}^2 d\Omega}}$$

to judge the accuracy of the SE methods. To compute the Courant number the elements are decomposed into their high-order (HO) grid points and these grid points form a fine grid which we refer to as the HO cells. The velocities and grid spacings are then defined at the centers of these cells. Using these definitions the Courant number is then defined as

$$\text{Courant number} = \max \left(\frac{C \Delta t}{\Delta s} \right)_{HO}^e \quad \forall e \in [1, \dots, N_e]$$

where

$$C = \begin{cases} U & \text{for case 1} \\ U + \sqrt{\phi} & \text{for cases 2, 3, 4, 5, and 6} \end{cases}$$

where C is the characteristic speed, $U = \sqrt{\mathbf{u} \cdot \mathbf{u}}$, and $\Delta s = \sqrt{\Delta x^2 + \Delta y^2 + \Delta z^2}$ is the grid spacing. For all the results presented the Courant number is taken to be 0.5.

Six test cases are used to judge the performance of the triangle-based SE method. Cases 1, 2, 3, 5, and 6 correspond to the Williamson et al. standard test case suite [24]. Case 4 was recently proposed by Galewsky et al. for testing shallow water models [6]. This case presents a more challenging test than those in the Williamson et al. test suite because if the resolution is not sufficiently high then the numerics will not be able to sustain the steady zonal jet with steep vorticity gradient. If the method cannot sustain the jet then the accuracy declines rapidly. Case 1 involves the geopotential equation (passive advection) only whereas the remainder of the test cases concern the full shallow water equations. In addition, cases 1, 2, 3, and 4 have analytic solutions whereas cases 5 and 6 do not and are only used to determine

the accuracy of the triangle-based SE method qualitatively. These last two test cases have been run by a vast community and the results are well-documented for comparison.

5.1. Description of the Test Cases

5.1.1. Case 1: Passive Advection of a Cosine Wave

Case 1 concerns the solid body rotation of a cosine wave. The velocity field remains unchanged throughout the computation. Williamson et al. [24] recommend that the error be computed after 12 days of integration which corresponds to one complete revolution of the cosine wave.

5.1.2. Case 2: Steady-State Nonlinear Zonal Geostrophic Flow

This case is a steady-state solution to the nonlinear shallow water equations. The equations are geostrophically balanced and remain so for the duration of the integration where the velocity field remains constant throughout the computation. The geopotential height ϕ undergoes a solid body rotation but since the initial height field is given as a constant band in the zonal direction and the flow field is purely zonal, then the solution remains unchanged throughout the time-integration. The velocity field is the same as that used in case 1. Williamson et al. [24] recommend that the error be computed after 5 days of integration.

5.1.3. Case 3: Steady-State Nonlinear Zonal Geostrophic Flow with Compact Support

This case is another steady-state solution to the nonlinear shallow water equations where the equations remain geostrophically balanced for the duration of the integration. The initial velocity field is zero everywhere except in a very small isolated region. This isolated region, or jet, encapsulates the flow and confines the geopotential height field to remain within a localized circular region. The results are reported for a 5-day integration as suggested in [24].

5.1.4. Case 4: Galewsky et al. Zonal Dynamics

This test case consists of a zonal jet and an unperturbed balanced initial geopotential height field. The balanced initial field should be maintained indefinitely but Galewsky et al. [6] suggest running the case for 5 days. This is a rather stringent test of shallow water models because if the accuracy and/or the resolution is not sufficiently high then the model will not be able to sustain the balanced initial field and the error will increase quite rapidly, unlike cases 1, 2, and 3 which are much more forgiving. In addition, because the jet is zonally positioned, then any grid that is not aligned with the zonal direction will have much more difficulty maintaining the jet.

5.1.5. Case 5: Zonal Flow over an Isolated Mountain

This case uses the same initial conditions as case 2 with the addition of a conical mountain at $(\lambda, \varphi) = (180, 30)$. Due to the zonal flow impinging on the mountain, various wave structures form and propagate throughout the sphere. This test is run for 15 days as suggested in [24].

5.1.6. Case 6: Rossby-Haurwitz Wave

Although Rossby-Haurwitz waves are not analytic solutions to the shallow water equations, they have become a *de facto* test case. In a non-divergent barotropic model, the initial geopotential height field undergoes a solid body rotation in a counterclockwise direction when viewed from the North Pole. Although this case does not have an analytic solution, it is well-known that the initial wave structure of the Rossby-Haurwitz wave should remain intact for the duration of the time-integration.

5.2. Results on the Test Case Suite

5.2.1. Convergence Rate of the Triangle-based SE Method

Before analyzing the behavior of the triangle-based SE method on the standard test case suite or delving into comparisons between the triangle-based SE method with the quadrilateral-based method it is important to quantify the convergence rate of the method. For this study we use case 2 and show convergence rates in Fig. 4 for $N = 1, 2, 4, 6, 8, 10, 12$ and 14. The order of convergence shown in Fig. 4

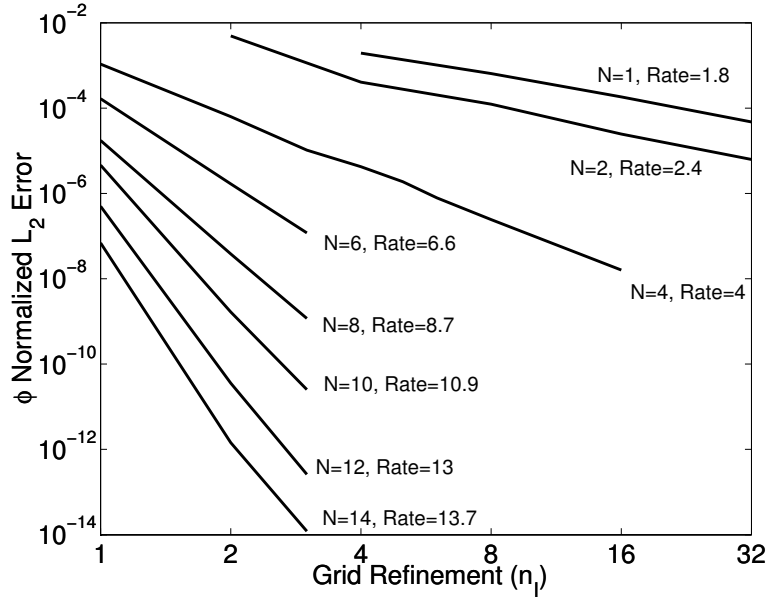


FIG. 4. Case 2. The normalized ϕ error norm as a function of icosahedral grid refinement, n_I , after 5 days for the polynomial orders $N = 1, 2, 4, 6, 8, 10, 12$, and 14 with their associated convergence rates.

is computed as an average convergence rate computed over all the grid refinements where at each grid refinement the convergence rate is defined as

$$\text{rate} = \frac{\log [\text{error}_{n_I+1} / \text{error}_{n_I}]}{\log [n_I / (n_I + 1)]}.$$

This figure shows that the expected spectral accuracy is achieved for all values of N , that is,

$$\text{error} \propto \mathcal{O}(\Delta x^{N+1})$$

which states that the error decreases exponentially with increasing N .

5.2.2. Case 1: Passive Advection of a Cosine Wave

Figure 5 shows that the SE method on triangles and quadrilaterals converge algebraically regardless of the structure of the grid. Exponential convergence is not expected for this case because the derivative at the base of the cosine hill is non-smooth. Note that the triangle-based and quadrilateral-based SE converge at approximately the same rate with the quadrilateral-based method being slightly better than the triangle-based method.

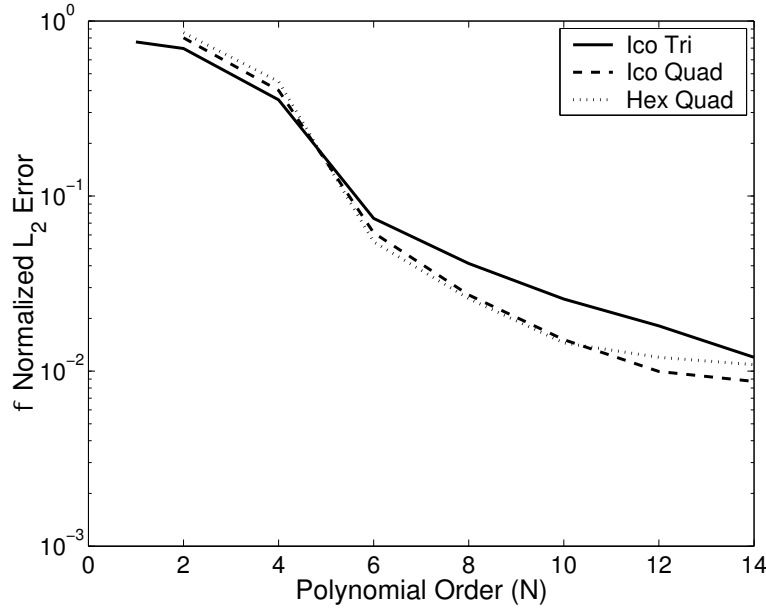


FIG. 5. Case 1. The normalized ϕ error norm as a function of polynomial order, N , after 12 days using 80, 60, and 54 elements for the icosahedral triangle-based (Ico Tri), icosahedral quadrilateral-based (Ico Quad), and hexahedral quadrilateral-based (Hex Quad) spectral elements.

5.2.3. Case 2: Steady-State Nonlinear Zonal Geostrophic Flow

Figure 6 illustrates that the triangle-based and quadrilateral-based SE methods yield exponential convergence. The quadrilateral-based hexahedral grid yields the best results with the triangle-based icosahedral grid giving better results than the quadrilateral-based icosahedral grid. The hexahedral grid will be very difficult to beat for this test case because it is aligned with the direction of the flow. For this reason it is expected that a latitude-longitude grid would also do extremely well for this test case.

5.2.4. Case 3: Steady-State Nonlinear Zonal Geostrophic Flow with Compact Support

Figure 7 shows that the triangle-based and quadrilateral-based SE methods, again, yield exponential convergence; however, the triangle-based SE method is slightly better than the quadrilateral-based SE methods. Unlike case 2, this case

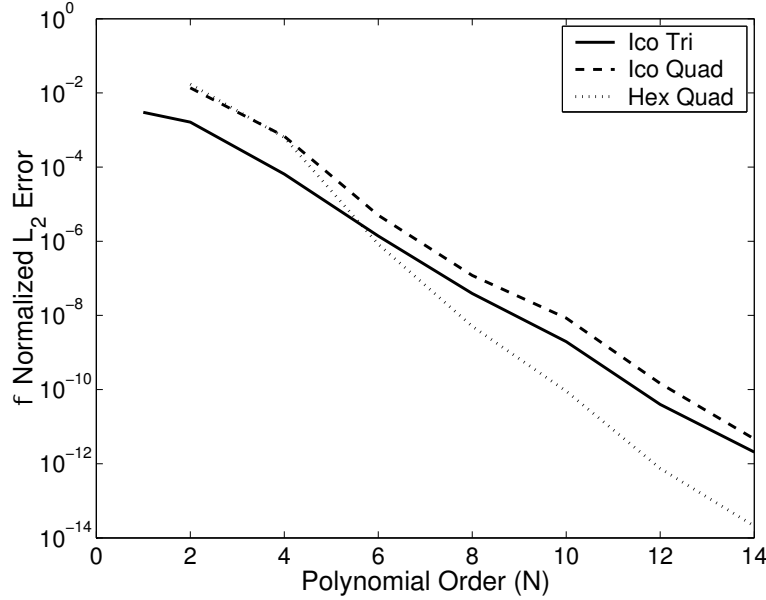


FIG. 6. Case 2. The normalized ϕ error norm as a function of polynomial order, N , after 5 days using 80, 60, and 54 elements for the icosahedral triangle-based (Ico Tri), icosahedral quadrilateral-based (Ico Quad), and hexahedral quadrilateral-based (Hex Quad) spectral elements.

represents a more localized flow problem. The circular region where the geopotential is confined is not aligned with any of the grids and so the isotropy of the grid becomes an important factor. This explains why the triangle-based SE method on the icosahedral grid yields better accuracy than the quadrilateral-based methods.

5.2.5. Case 4: Galewsky et al. Zonal Dynamics

Figure 8 illustrates the convergence rates of the triangle-based and quadrilateral-based SE methods as a function of total number of grid points, N_p , with 8th order polynomials. This figure shows that triangle-based and quadrilateral-based SE methods yield high-order convergence and that the triangle-based SE method is superior to the quadrilateral-based SE methods. Once again, the absence of grid alignment with the flow has hindered the quadrilateral-based SE methods from resolving the physics of the problem as well as the more isotropic triangle-based icosahedral grid. Figures 9 and 10 show snapshots of the grid, geopotential (ϕ), and zonal velocity (u_s) after a 5-day integration for the triangle-based and quadrilateral-based SE methods with various grid resolutions using 8th order polynomials. The view of the figures is from the North Pole. In Fig. 9 it is observed that the resolutions $n_I = 3$ ($N_p = 5762$) and $n_I = 4$ ($N_p = 10242$) are not capable of maintaining the jet. The formation of wave number 5 structures begin to emerge due to the lack of symmetry in the grid near the initial points of the icosahedron (which form a pentagon around the pole). For $n_I = 5$ ($N_p = 16002$) the balanced initial state is maintained where the jet is visibly intact. Similarly, Fig. 10 shows that the quadrilateral-based SE method on the hexahedral grid cannot maintain the jet for resolutions $N_p < 38402$. Thus the triangle-based SE method on icosahedral grids

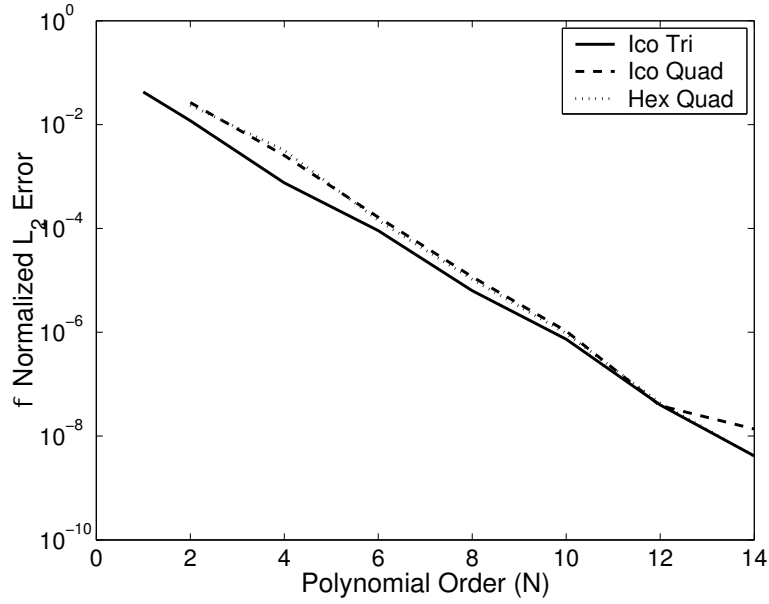


FIG. 7. Case 3. The normalized ϕ error norm as a function of polynomial order, N , after 5 days using 80, 60, and 54 elements for the icosahedral triangle-based (Ico Tri), icosahedral quadrilateral-based (Ico Quad), and hexahedral quadrilateral-based (Hex Quad) spectral elements.

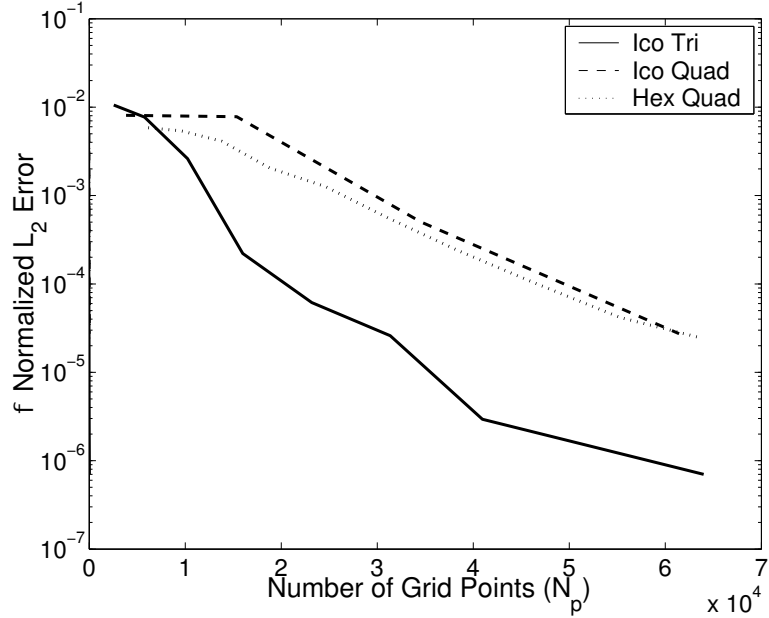


FIG. 8. Case 4. The normalized ϕ error norm as a function of grid points, N_p after 5 days using $N = 8$ for the icosahedral triangle-based (Ico Tri), icosahedral quadrilateral-based (Ico Quad), and hexahedral quadrilateral-based (Hex Quad) spectral elements.

can maintain the jet with 58% fewer points than the quadrilateral-based SE method on hexahedral grids.

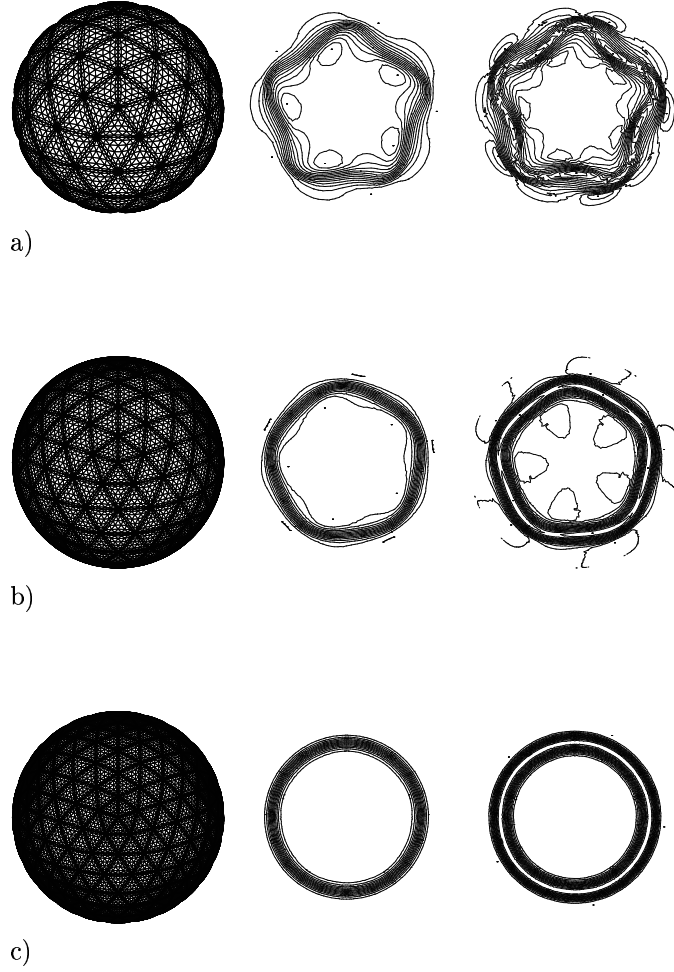


FIG. 9. Case 4. Contours of the grid (left), ϕ (center), and u_s (right) for the triangle-based SE method after 5 days for $N = 8$ and a) $n_I = 3$ ($N_p = 5762$), b) $n_I = 4$ ($N_p = 10242$), and c) $n_I = 5$ ($N_p = 16002$) viewed from the North Pole.

5.2.6. Case 5: Zonal Flow over an Isolated Mountain

Figure 11 shows snapshots of the fields after a 15-day integration for various grid resolutions (with $N = 8$). The view of the figures is from $(\lambda, \varphi) = (180, 0)$. All three grid resolutions show the correct wave structures but the curves are much smoother for increasing resolution.

5.2.7. Case 6: Rossby-Haurwitz Wave

Figure 12 shows snapshots of the fields after a 14-day integration for various grid resolutions (with $N = 8$). The view of the figures is from the North Pole. All three grid resolutions show the correct wave structures with the contours becoming sharper with increasing resolution.

5.2.8. The Advantages of using Adaptive Unstructured Triangular Grids

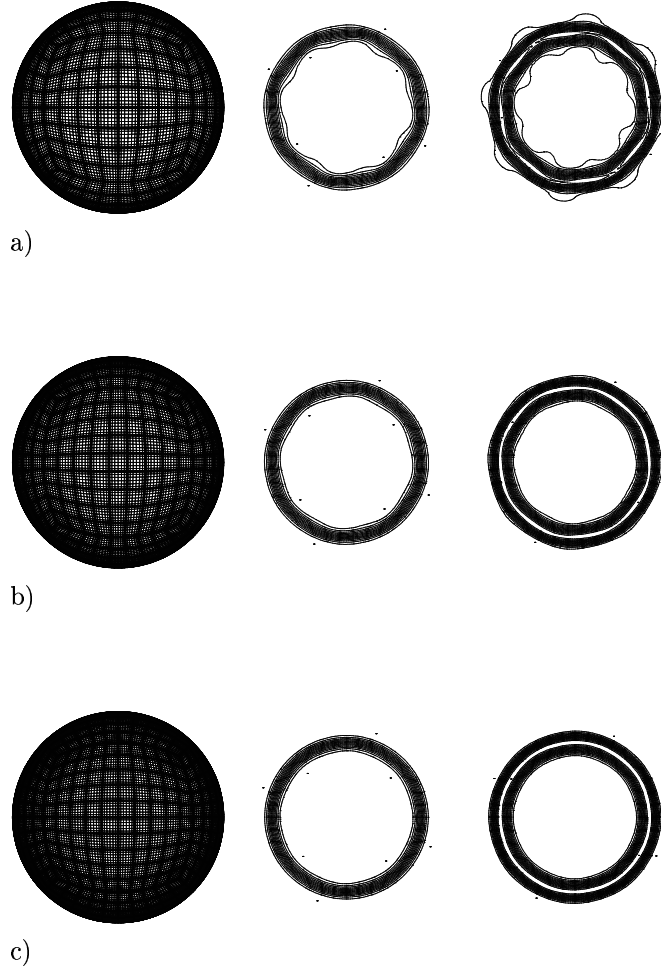


FIG. 10. Case 4. Contours of the grid (left), ϕ (center), and u_s (right) for the quadrilateral-based SE method after 5 days for $N = 8$ and a) $n_H^Q = 8$ ($N_p = 24578$), b) $n_H^Q = 9$ ($N_p = 31106$), and c) $n_H^Q = 10$ ($N_p = 38402$) viewed from the North Pole.

To show the advantages that adaptive unstructured triangular grids may offer we revisit case 1. For this test case the quadrilateral-based hexahedral grid yielded a superior convergence rate to the triangle-based SE method on icosahedral grids. It was conjectured that the alignment of the hexahedral grid with the direction of the flow accounted for this difference in convergence rates. Therefore, let us now compute the convergence rate for the triangle-based SE method on an adaptive unstructured grid aligned with the flow direction. Figure 13 shows the grid (with $N = 8$) and the contours of ϕ after one revolution. Figure 14 shows that the convergence rate for the triangle-based SE method on the adaptive grid is now superior to that of the quadrilateral-based SE method on both the hexahedral and icosahedral grids. It should be mentioned that all three grids have approximately the same number of grid points. Constructing this type of grid with the quadrilateral-based SE method is not possible.

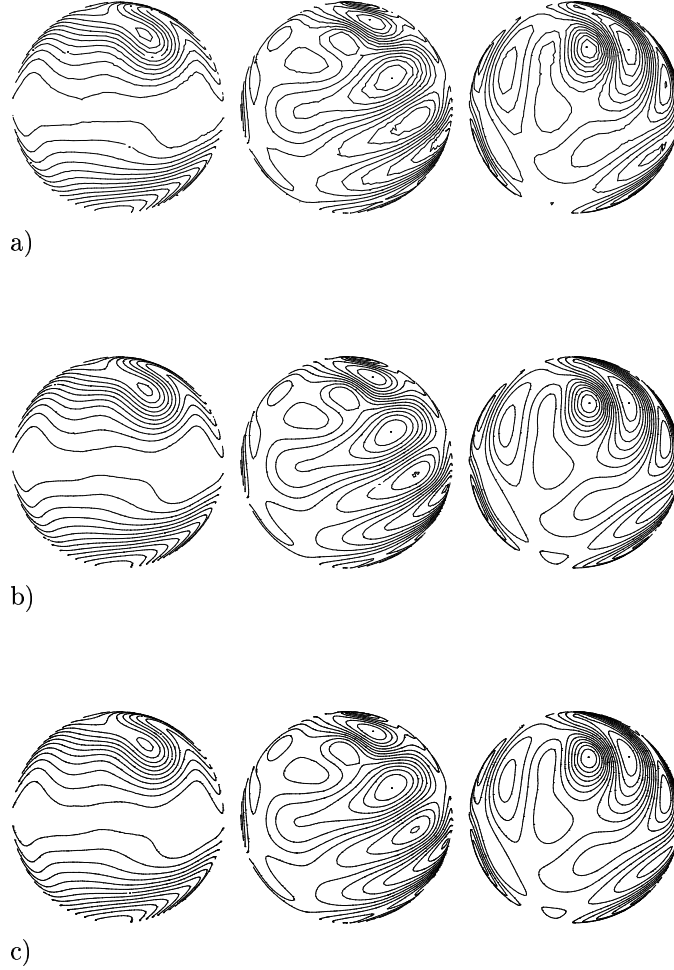


FIG. 11. Case 5. Contours of ϕ (left), u_s (center), and v_s (right) for the triangle-based SE method after 15 days for $N = 8$ and a) $n_I = 2$, b) $n_I = 4$, and c) $n_I = 6$ viewed from $(180, 0)$ which is in the vicinity of the mountain.

6. CONCLUSIONS

The newly proposed triangle-based SE method exhibited its expected exponential convergence. Furthermore, the triangle-based SE method was shown to be superior to the quadrilateral-based methods for three of the four cases having analytic solutions. Cases 5 and 6 have been typically used to represent challenging cases but the triangle-based SE method was capable of representing the underlying physics of these problems with a modest grid resolution. However, case 4 showed that for crude resolutions, the wave structure collapses therefore representing a good addition to the Williamson et al. shallow water test case suite. For cases 1 and 2, the quadrilateral-based SE method on hexahedral grids was shown to be superior to the triangle-based SE method on icosahedral grids. These cases, however, represent flows which are aligned with the hexahedral grid and for this reason it is difficult to compete with the quadrilateral-based SE method. However, with the assistance of

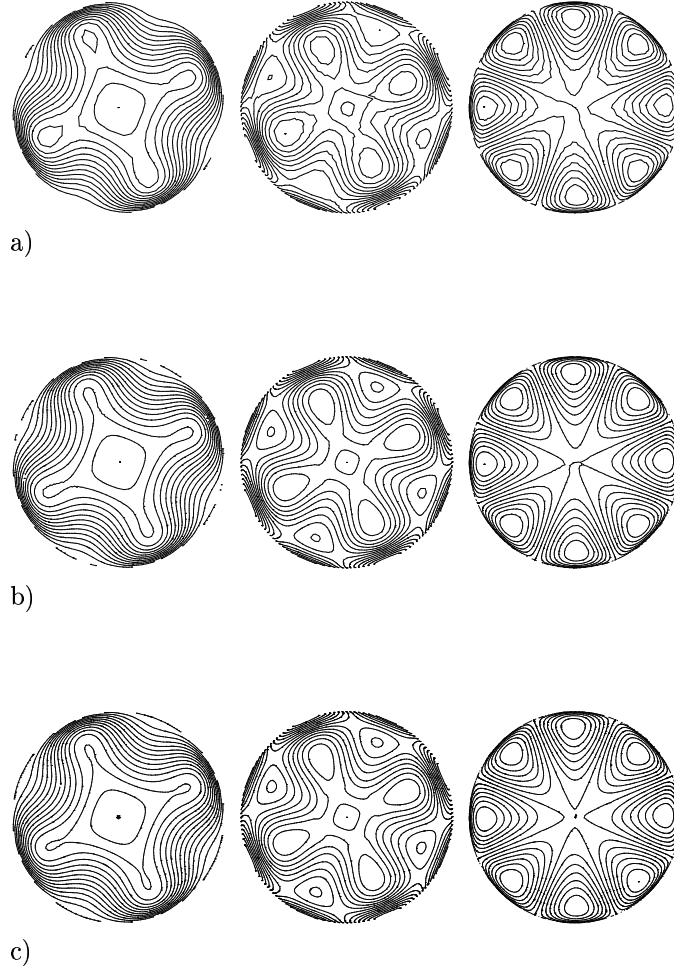


FIG. 12. Case 6. Contours of ϕ (left), u_s (center), and v_s (right) for the triangle-based SE method after 14 days for $N = 8$ and a) $n_I = 2$, b) $n_I = 4$, and c) $n_I = 6$ viewed from the North Pole.

an adaptive unstructured grid, the triangle-based SE method proved to be superior. Cases 3 and 4 have strong local characteristics whereby the geopotential height is confined within a small circular region encapsulated by a jet. For these cases, the hexahedral grid is no longer aligned with the predominant features of the flow. It is conjectured that the isotropy of the triangle-based SE method on the icosahedral grid is what allows the triangle-based SE method to achieve a better convergence rate than the quadrilateral-based SE methods. The success of the triangle-based SE method for these two test cases are encouraging because it implies that while the method can accurately handle flows with strong global features it is much better suited for handling flows with significant local characteristics. It is therefore a good candidate for use with adaptive grids as was shown for case 1.

It should be mentioned that we have not shown performance comparisons between the triangle-based and quadrilateral-based methods. At the present the quadrilateral-based SE method is at a far more mature stage than its triangle-

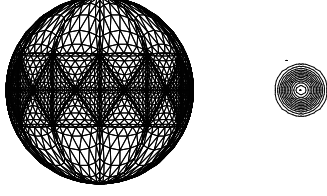


FIG. 13. Case 1. The grid (left) and contours of ϕ (right) for the triangle-based SE method for $N = 8$.

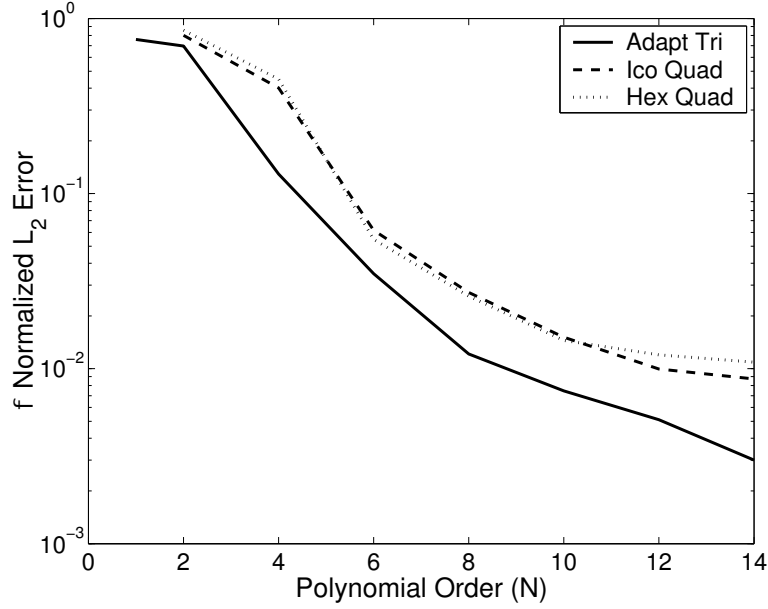


FIG. 14. Case 1. The normalized ϕ error norm as a function of polynomial order, N , after 12 days using 92, 60, and 54 elements for the adaptive latitude-longitude triangle-based (Adapt Tri), icosahedral quadrilateral-based (Ico Quad), and hexahedral quadrilateral-based (Hex Quad) spectral elements.

based counterpart. Unlike the quadrilateral-based SE method, the triangle-based SE method does not give rise to a diagonal mass matrix, M , and thereby requires inverting a sparse global matrix at each time step. Even though the triangle-based SE method requires 30% to 60% fewer grid points than its quadrilateral-based counterpart to achieve the same accuracy, the inversion of a global matrix significantly reduces the efficiency of the triangle-based method. In this paper we have only presented the triangle-based SE method in its continuous form, in the future we shall explore this method in its discontinuous form which eliminates the

need for inverting a global matrix. We will also consider more efficient domain decomposition techniques which will improve the apparent inefficiency in the current approach. The exponential accuracy and geometric flexibility of the triangle-based SE method merits further investigations into implementing it to the primitive atmospheric equations.

ACKNOWLEDGMENT

FXG was supported by the Office of Naval Research through program element PE-0602435N. TW was supported by NSF under contract ITR-0321911, through the Sandia University Research Program, and by ARO under contract DAAD19-03-1-0146.

REFERENCES

1. J. Behrens, AMATOS - adaptive mesh generation for atmospheric and ocean simulations, Munich Technical University, Center for Mathematical Sciences, D-80290 Munich, Germany (2002), API Documentation version 1.2.
2. J. Boyd, The erfc-log filter and the asymptotics of the Euler and Vandeven sequence accelerations, *Houston Journal of Mathematics* (1996).
3. R. Cools, and P. Rabinowitz, Monomial cubature rules since Stroud: A compilation, *Journal of Computational and Applied Math*, **48**, 309-326, (1993).
4. R. Cools, Monomial cubature rules since Stroud: A compilation - Part 2, *Journal of Computational and Applied Math*, **112**, 21-27, (1999).
5. M. Dubiner, Spectral methods on triangles and other domains, *Journal of Scientific Computing* **6**, 345-390 (1991).
6. J. Galewsky, R.K. Scott, and L.M. Polvani, An initial-value problem for testing numerical models of the global shallow water equations, *Tellus* in press (2004).
7. F.X. Giraldo, Lagrange-Galerkin methods on spherical geodesic grids: the shallow water equations, *Journal of Computational Physics* **160**, 336-368 (2000).
8. F.X. Giraldo, The Lagrange-Galerkin method for the 2D shallow water equations on adaptive grids, *International Journal for Numerical Methods in Fluids* **33**, 789-832 (2000).
9. F.X. Giraldo, A spectral element shallow water on spherical geodesic grids, *International Journal for Numerical Methods in Fluids* **35**, 869-901 (2001).
10. F.X. Giraldo, J.S. Hesthaven, and T. Warburton, Nodal high-order discontinuous Galerkin methods for the spherical shallow water equations, *Journal of Computational Physics* **181**, 499-525 (2002).
11. F.X. Giraldo, J.B. Perot, and P.F. Fischer, A spectral element semi-Lagrangian (SESL) method for the spherical shallow water equations, *Journal of Computational Physics* **190**, 623-650 (2003).
12. F.X. Giraldo and T.E. Rosmond, A scalable spectral element Eulerian atmospheric model for NWP: dynamical core test, *Monthly Weather Review* **132**, 133-153 (2004).
13. F.X. Giraldo, Semi-implicit time-integrators for a scalable spectral element atmospheric model, *Quarterly Journal of the Royal Meteorological Society* submitted (2003).
14. T. Heinze and A. Hense, The shallow water equations on the sphere and their Lagrange-Galerkin solution, *Meteorology and Atmospheric Physics* **81**, 129-137 (2002).
15. R.D. Henderson and G.E. Karniadakis, Unstructured spectral element methods for simulation of turbulent flows, *Journal of Computational Physics* **122**, 191-217 (1995).
16. J.S. Hesthaven, From electrostatics to almost optimal nodal sets for polynomial interpolation in a simplex, *SIAM Journal on Numerical Analysis* **35**, 655-676 (1998).
17. T. Koornwinder, Two-variable analogues of the classical orthogonal polynomials, in *Theory and Applications of Special Functions*, edited by A.R.A. (Academic Press, San Diego, 1975).
18. R. J. Renka, Algorithm 772. STRIPACK: Delaunay triangulation and voronoi diagram on the surface of a sphere, *ACM Trans. Math. Software*, **23**, 416-434 (1997).

19. S.J. Sherwin and G.E. Karniadakis, A triangular spectral element method; applications to the incompressible Navier-Stokes equations, *Computer Methods in Applied Mechanics and Engineering* **123**, 189-229 (1995).
20. A.H. Stroud, Approximate Calculation of Multiple Integrals, Prentice-Hall Publishing, New Jersey, (1971).
21. P.N. Swarztrauber, D.L. Williamson, and J.B. Drake, The Cartesian method for solving partial differential equations in spherical geometry, *Dynamics of Atmospheres and Oceans* **27**, 679-706 (1997).
22. M.A. Taylor, B.A. Wingate, and R.E. Vincent, An algorithm for computing Fekete points in the triangle, *SIAM Journal on Numerical Analysis* **38**, 1707-1720 (2000).
23. T. Warburton, L.F. Pavarino, and J.S. Hesthaven, A pseudo-spectral scheme for the incompressible Navier-Stokes equations using unstructured nodal elements, *Journal of Computational Physics* **164**, 1-21 (2000).
24. D.L. Williamson, J.B. Drake, J.J. Hack, R. Jakob, and P.N. Swarztrauber, A standard test set for numerical approximations to the shallow water equations in spherical geometry, *Journal of Computational Physics* **102**, 211-224 (1992).